Scenario and Model Dependence of Strategic Solar Climate Intervention in CESM

J. T. Fasullo[1] and J. H. Richter[1]

[1]National Center for Atmospheric Research, Boulder, CO, 80301.

Corresponding author: Dr. John Fasullo (fasullo@ucar.edu)

Key Points:

- A substantial contrast in the meridional structure of stratospheric aerosols exists in two recent climate intervention experiments.
- Differences in the representations of clouds and the Atlantic Meridional Overturning Circulation are identified as key drivers of the contrast.
- The results portend significant uncertainty in the distribution of sulfate gas injections associated with strategic climate intervention.

Abstract

Model dependence in simulated responses to stratospheric aerosol injection (SAI) is a major uncertainty surrounding the potential implementation of this solar climate intervention strategy. We identify large differences in the aerosol mass latitudinal distributions between two recently produced climate model SAI large ensembles, despite using similar climate targets and controller algorithms, with the goal of understanding the drivers of such differences. Using a hierarchy of recently produced simulations, we identify three main contributors including: 1) the rapid adjustment of clouds and rainfall to elevated levels of carbon dioxide, 2) the associated low-frequency dynamical responses in the Atlantic Meridional Overturning Circulation, and 3) the contrasts in future climate forcing scenarios. Each uncertainty is unlikely to be significantly narrowed over the likely timeframe of a potential SAI deployment if a 1.5C target is to be met. The results thus suggest the need for significant flexibility in climate intervention deployment in order to account for these large uncertainties in the climate system response.

Plain Language Summary

The continued high levels of anthropogenic greenhouse gas emissions increase the likelihood that key climate warming thresholds will be exceeded in the coming decades unless some form of climate intervention is implemented. It is in this context that we examine a recently proposed approach to stratospheric aerosol injection. Using two recently produced climate model experiments, we find the associated latitudinal distribution of aerosol mass to exhibit substantial uncertainty, suggesting the need for significant flexibility in the location and amount of aerosol delivery. The uncertainty's origins stem mainly from simulated climate responses to increases in carbon dioxide including rapid adjustments in clouds and rainfall, and changes in the overturning ocean circulation. Uncertainty in future anthropogenic emissions of industrial sulfate aerosols also contribute.

1 Introduction

Solar climate intervention (SCI), or solar geoengineering, has been proposed as a means of reducing the adverse impacts of climate change via the artificial enhancement of Earth's albedo. One SCI method proposed to temporarily offset anthropogenic warming and associated impacts is stratospheric aerosol injection (SAI), which involves the delivery of aerosols or precursor gases into the stratosphere. A major uncertainty surrounding the enactment of SAI is the climate system response to both continued emissions of carbon dioxide and prolonged elevated levels of stratospheric sulfate aerosols.

It is in the context of this uncertainty that the National Academies of Sciences, Engineering, and Medicine (NASEM) recently called for further research to understand various SCI approaches (NASEM, 2021) as SAI has been shown, in principle, to be a method of global climate intervention capable of achieving various temperature-based targets (Tilmes et al. 2018, MacMartin et al. 2019, Simpson et al. 2019). However, there remain large uncertainties in associated climate responses and impacts (Fasullo et al. 2018, Kravitz and MacMartin 2020) and adverse effects have been identified involving the water cycle and circulations in the troposphere, stratosphere, and ocean (Tilmes et al. 2018, Kawatani et al. 2011, Watanabe and Kawatani 2012, Fasullo et al. 2018, Xu et al. 2020, Xie et al. 2021, Sun et al. 2020, Abiodun et al. 2021, Banerjee et al. 2021 Krishnamohan and Bala 2022).

Climate models are an essential tool for exploring the potential benefits and impacts of the broad range of proposed SAI approaches. They depict the interactions between multiple processes involved in the climate response and simulate impact-relevant fields. They also provide a process-based understanding of response mechanisms and timescales. Due to the large internal variability of the climate system, the evaluation of SAI approaches often requires climate model large ensembles (Deser et al., 2012, Kay et al. 2015, Maher et al. 2021) using Earth system models (ESMs) capable of accurately representing a diverse set of processes involving stratospheric and tropospheric dynamics and chemistry, and time-varying aerosol distributions, aspects that are well-represented in only a few currently available ESMs (Franke et al. 2021).

While some recent work has found broad consistency in simulated responses to simple SAI depictions, such as solar dimming (e.g. Kravitz et al. 2021, Visioni et al. 2021), this work identifies and explores substantial climate response dependencies to a more realistic SAI representation based on explicitly resolved stratospheric aerosol injections, their evolving aerosol size distributions and burdens, their interactions with dynamical, chemical, and hydrologic processes, and related couplings between the land, atmosphere, ocean, and cryosphere (MacMartin et al. 2017, Tilmes et al. 2018, Richter et al. 2022). In this work, we explore the origin of inter-model differences and their physical bases. The models, experiments, and methods used are described in Section 2. The spatial and temporal structure of injected aerosols and climate responses are presented and discussed in Section 3 while the broader consequences for the potential implementation of SAI, and suggestions for future work, are presented in Section 4.

2 Materials and Methods

2.1 Models

With the goal of explicitly representing the dynamical, chemical, and hydrological aspects of the climate response to SAI, this work uses versions 1 and 2 of the Community Earth System Model (CESM1, CESM2). Both versions can be run in so-called high-top and low-top atmospheric configurations. The CESM1 high-top configuration uses the Whole Atmosphere Community Climate Model, version 5 (CESM1-WACCM5, Mills et al., 2017) as its atmospheric component and the CESM2 uses WACCM6 (CESM2-WACCM6, Gettelman et al. 2019). For the atmosphere, CESM1-WACCM5 has zonal and meridional resolutions of 0.9° and 1.25°, respectively, with 70 vertical levels and a model top of 140 km. The configuration allows for a full representation of stratospheric dynamics and has extensive middle atmospheric chemistry, and is a key improvement upon earlier model generations and many current climate models (e.g., Ferraro et al., 2015). Tropospheric physics in WACCM5 are the same as in the lower top configuration, the Community Atmosphere Model version 5 (CAM5, Park et al. 2014), the atmospheric component of the CESM1 (Hurrell et al. 2013). CESM1-WACCM5 explicitly simulates sulfate aerosol concentrations and size distributions via the Modal Aerosol Module (MAM3; Mills et al., 2017). Associated responses in ozone concentrations have a beneficial impact on the stratospheric circulation and its biennial variability (Richter et al., 2017) and these have been shown to reduce the CO_2-driven midlatitude jets' poleward shift under present-day climate change (Chiodo and Polvani, 2019). Confidence in the representations of sulfate aerosol processes and their radiative effects are bolstered by the relatively close agreement that exists between simulated and observed radiative responses to the 1991 eruption of Mount Pinatubo (Mills et al., 2017). The ocean component of all models used in this study is the Parallel Ocean

Program version 2 (POP2; Smith et al., 2010; Danabasoglu et al., 2012), which as uniform zonal resolution of 1.125º, and variable meridional resolution ranging from 0.27° in the tropics to 0.64° in the extratropical northern hemisphere. The model has 60 vertical levels with a uniform resolution of 10 m in the ocean's upper 160 m.

CESM2-WACCM6 incorporates various advances including fully interactive tropospheric chemistry and an interactive crop model. Tropospheric physics is largely the same as in the low-top configuration, the Community Atmosphere Model version 6 (CAM6) as a concerted effort was made during development of these models to use the same model tuning in the low-top and high-top configurations in order to promote inter-version comparison (Gettelman et al. 2019). CAM6 is the atmospheric component of CESM2 (Danabasoglu et al. .2020) and uses the Cloud Layers Unified By Binormals (CLUBB; Golaz et al., 2002; Larson, 2017) unified turbulence scheme and the updated Morrison-Gettelman microphysics scheme (MG2; Gettelman and Morrison, 2015). Minor changes to POP2 are incorporated in CESM2-WACCM6 (Danabasoglu et al., 2020).

2.2 CESM1-WACCM5 Simulations

A summary of design characteristics for the simulations used here are given in Table 1. We use CESM1-WACCM5 SAI simulations that are a part of the Geoengineering Large Ensemble (GLENS, Tilmes et al., 2018). GLENS consists of two large ensemble of simulations: one without and one with SAI. Both ensembles use the Representative Concentration Pathway 8.5 (RCP85) emissions scenario for greenhouse gases. The baseline GLENS simulations consists of free running RCP85 simulations from 2005 through 2030 (17 members), with an additional 3 members continuing through 2100 (CESM1-WACCM5-RCP85). The second set of GLENS simulations, GLENS-SAI, utilizes strategically enacted SAI (following Kravitz et al. 2017), which consists of twenty members from 2020 to 2097 in which aerosol injections are specified by a controller algorithm (MacMartin et al. 2014, Kravitz et al. 2017) to achieve stabilization of temperature targets at their mean 2020 conditions under RCP85. The targets include near-surface air temperature's global mean, equator-to-pole gradient, and inter-hemispheric gradient, which are all successfully stabilized in GLENS-SAI, though the equator-to-pole gradient increases slightly (by about 0.1 K from 2050 to 2070, Tilmes et al. 2018). The predefined injection latitudes for GLENS-SAI are 15º and 30º in each hemisphere and SO_2 is injected about 5 km above the tropopause, or approximately 25 and 23 km for the 15º and 30º sites, respectively, with an arbitrarily chosen longitude of 180º (Tilmes et al. 2018). The initialization of GLENS-SAI is made from three distinct members of the RCP85 experiment, which itself branched from distinct historical-era simulations, thus providing a diversity of initialized ocean states. GLENS has been used in a range of contexts (Fasullo et al. 2018, Simpson et al. 2019, Pinto et al., 2020, Da-Allada et al, 2020).

2.3 CESM2-WACCM6 Simulations

As with GLENS, we use two sets of CESM2-WACCM6 experiments.The CESM2-WACCM6 baseline simulations used are from the Coupled Model Intercomparison Project version 6 (CMIP6, Eyring et al. 2016) and the Assessing Responses and Impacts of Solar climate intervention on the Earth system with Stratospheric Aerosol Injection project ARISE-SAI, Richter et al. 2022). These include the unmitigated CMIP6 SSP585 simulations, to allow for comparison with the RCP85 experiments in GLENS (Tilmes et al. 2020). The second experiment

used is the SAI ensemble, with strategically placed sulfur dioxide injection to keep the global mean temperature at ~ 1.5 C over preindustrial temperatures (ARISE-SAI-1.5, Richter et al. 2022). These simulations extend from 2035 to 2069 and use the same controller algorithm and target metrics as GLENS-SAI, but for the 2020-2039 time average in the unmitigated CESM2-WACCM6 baseline simulations, in contrast to GLENS-SAI where targets are based on the 2010 – 2030 time period. Target metrics are successfully met in ARISE-SAI-1.5 to within 0.05 K over the period 2050 to 2070 (Richter et al. 2022). The injections are again at 15° and 30 ° in both hemispheres and at an arbitrarily chosen longitude of 180°, as in GLENS-SAI, but occur lower in the stratosphere (approximately 21 km). The slight difference in injection height between GLENS-SAI and ARISE-SAI doesn't significantly impact their efficacy however as the shortwave optical depth of the stratosphere is small relative to the troposphere. Moreover, single point injections result in strong similarity in the latitudinal structure of aerosol optical depth between CESM1 (Tilmes et al., 2017) and CESM2 (Visioni et al., 2022), with circulation differences and lifetime effects contributing to slightly greater aersol optical depths in GLENS (Visioni et al. 2022). ARISE-SAI-1.5 simulations use the moderate Shared Socioeconomic Pathway (SSP) scenario of SSP245 for its defacto future scenario (Burgess et al., 2020), a moderate scenario where "the world follows a path in which social, economic, and technological trends do not shift markedly from historical patterns" (O'Neill et al. 2016). The temperature targets for ARISE-SAI-1.5 are based on the same regional metrics as used in GLENS-SAI and the simulations consist of a 10-member ensemble.

2.4 Additional Simulations

In order to gain insight into the drivers of contrasts between the above SAI simulations, we use additional experiments. Below the stratosphere, CAM5 and CAM6 use physical representations of the climate system that are highly similar to their WACCM counterparts. Simulations using them therefore provide a means for inferring the troposperhic contribution to contrasts in our SAI experiments. For example, the ensemble mean of the CESM1 and CESM2 large ensembles (LE) provides an estimate of the future forced response (to both warming and CO_2 increases) by averaging across members, and through internally driven variability. Simulations used here include the 40-member CESM1-LE (Kay et al. 2015) and 100-member CESM2-LE (Rodgers et al. 2021), and a 10-member ensemble of CESM2 that makes use of CMIP5 historical and RCP85 prescribed forcing agents, (CESM2-RCP85, Forster et al. 2013). These large ensembles extend from 1850 to 2100, though for the CESM1-LE and CESM2-RCP85 only a single member spans 1850-1920. Also notable is the fact that the CESM2-LE uses SSP370 for its future scenario, rather than the SSP245 used in ARISE or the SSP585 used in future CESM2-WACCM6 simulations, and these differences complicate direct comparisons, as discussed further below. SSP370 represents the medium to high end of plausible future pathways and represents a forcing level common to several unmitigated SSP baselines

To quantify rapid adjustments to CO_2, those that occur in the absence of surface warming (e.g. Tilmes et al. 2013), idealized experiments using CESM1 and CESM2 are also used in which CO_2 is quadruped in both fixed sea surface temperature (SST, 4xCO2AMIP) and coupled ocean (Abrupt4xCO_2) frameworks. Conversely, slow reponses to warming are those that ensue in response to surface warming when CO_2 levels and other climate forcing agents are fixed, and these are estimated from so-called AMIP+4K experiments where uniform SST increases of 4 K are imposed on an AMIP background state. For these sensitivity experiments, the accompanying AMIP and pre-industrial coupled experiments are used to estimate 'control' conditions.

Together, these simulations allow for the estimation of both so-called "rapid adjustments" to CO_2 and "slow responses" to warming, and these are found to provide important insight into contrasts between GLENS and ARISE. Rapid adjustments also exist for other climate forcings, such as aerosols, and in the stratosphere these effects can be significant locally (Richter et al. 2017). On planetary scales however these have been shown generally to be small relative to the adjustment to CO_2 (Andrews et al., 2009; Bala et al., 2010; Samset et al., 2016; Tilmes et al., 2013).

3 Results

The yearly stratospheric aerosol mass injections specified in GLENS-SAI and ARISE-SAI-1.5 are shown in Figure 1, where we examine the common period of 2035 to 2069 (Table 1). The greater total emissions in GLENS-SAI than ARISE-SAI-1.5 are expected as they correspond to greater total offset CO_2 concentrations. However less expected is the large disparity in the latitudinal distribution of injections, with the vast majority of GLENS-SAI aerosols injected at 30°N and 30°S, with modest injection amounts occurring at 15°N and negligible injection mass at 15°S. This contrasts starkly with ARISE-SAI-1.5, where injections occur overwhelmingly at 15°S, with much smaller injection amounts at 15°N and 30°S, and negligible injection mass at 30°N. These relative proportions and their contrasts are approximately constant over time from 2035 to 2069, suggesting that they are relatively insensitive to the associated total avoided warming or the control period used for climate targets. Rather the persistence of the distributions over time suggests the possibility of an intrinsic contrast in the climate responses between the two ensembles.

To explore the processes that may underlie the contrasts in Fig. 1, the normalized structure of warming in a range of additionl simulations is examined in Figure 2. Normalized warming patterns from 2020-39 and 2050-69 in the associated unmitigated simulations (i.e. CESM1-WACCM5-RCP85 and CESM2-WACCM6-SSP585) show various features expected under anthropogenic climate change such as greater warming over land and in polar regions (Fig. 2a, b). Differences between the experiments are also clearly evident, particularly in the northern hemisphere (NH) extratropics, where warming is stronger in CESM1-WACCM5-RCP85 and a strong cooling in the North Atlantic (NATL) is evident in CESM2-WACCM6-SSP585. Differencing the normalized warming patterns (Fig. 2c) highlights systematically weaker warming in the NH in CESM2-WACCM6-SSP585 and stronger warming in the southern hemisphere (SH) subtropics, particularly in the subtropical stratocumulus cloud deck regions in the eastern ocean basins. When the analogous difference is computed between the CESM1-LE and CESM2-LE (Fig. 2d) a similar overall pattern emerges, albeit with slightly weaker magnitudes in the extratropical NH and SH. The strong similarities of patterns in Fig. 2c/d suggest a potentially dominant contribution from tropospheric physics in CAM5 and CAM6, which as discussed earlier are shared by their WACCM counterparts. The existence of differences between Figs. 2c/d suggests a potential role for both WACCM physics and scenario contrasts between the ensembles. The role of scenario can be estimated by examining differences between CESM2-RCP85 and CESM2-LE (Fig. 2e, note the scaling used). The persisting negative differences in the NH and positive differences in the SH subtropics suggest that the contrasts between SSP370, which is the future scenario used for the CESM2-LE (Fig. 2d), and RCP85 contribute to the pattern in Fig. 2d but are not the dominant contributor to it. Given this, potential contributors to the pattern are explored further below. Also notable is the result that various features of the unmitigated warming contrast between CESM1-WACCM5-RCP85 and CESM2-WACCM6-SSP585 (Fig. 2c) are shared by the differences in SAI regional warming

patterns (Fig. 2f), such as the elevated warming in the southern subtropics, and relative cooling in the NATL and NH subpolar regions, in ARISE-SAI-1.5 relative to GLENS-SAI, suggesting that these features may be intrinsic model responses.

To further explore the origin of model responses, changes in top-of-atmosphere (TOA) absorbed solar radiation (FSNT) are assessed and found to be strongly tied to patterns of warming. In unmitigated CESM1-WACCM5-RCP85 and CESM2-WACCM6-SSP585 simulations (Fig. 3a, b) normalized increases in FSNT are widespread, consistent with 21st century climate projections generally (Trenberth and Fasullo, 2009). However the inter-model difference (Fig. 3c) shows a strong spatial correlation with contrasting patterns of warming (Fig. 2c) as stronger SH subtropical warming in CESM1-WACCM5-RCP85 is accompanied by disproportionate FSNT increases while enhanced NATL cooling is coincident with FSNT decreases. When normalized patterns in the CESM1-LE and CESM2-LE are compared (Fig. 3d), a similar general pattern of FSNT differences exists, albeit slightly weaker, again suggesting the patterns to be an intrinsic feature of CAM5 and CAM6, with a potential secondary contribution from WACCM or scenario contrasts. When the CESM2-LE is compared to CESM2-RCP85 a similar but significantly weaker pattern of differences is evident (Fig. 3e, note the scaling used), suggesting a modest but detectible role for the future scenario in driving contrasts between the simulations. Unlike the temperature response under SAI, the difference pattern of FSNT change beween ARISE-SAI-1.5 and GLENS-SAI is not strongly correlated with that of the unmitigated simulations and instead largely reflects the combined and complex influence of changes in clouds and SAI (Fig. 3f).

Various additional analyses provide important background for interpreting contrasts in our SAI experiments. In Fig. 3, a focus on changes in patterns of FSNT is motivated by their dominant contribution to the overall pattern of net TOA flux (Fig. S1). While changes in outgoing longwave radiation exist (Fig. S2), these can generally be viewed as responding to differences in warming, rather than driving them, as they are positively correlated to temperature anomalies and thus offset, in many cases, changes in FSNT. Understanding the origin of spatial patterns and interhemispheric FSNT gradients in unmitigated simulations is therefore critical to anticipating the latitudinal distribution of injection amounts under SAI.

In this context the 4xCO2AMIP and Abrupt4xCO_2 simulations provide important insight as they demonstrate that responses in shortwave radiation and clouds to elevated levels of CO_2 (i.e. rapid adjustments) also differ considerably between CESM1 and CESM2 in a way that is consistent with the need for greater NH mitigation in the GLENS-SAI experiment. For example, in CESM1 there is a strong hemispheric gradient in FSNT rapid adjustments (Fig. 4) such that the NH absorbs 2.4 W m^{-2} more energy than the SH in response to a CO_2 quadruping. In contrast, in CESM2 the response is relatively symmetric between hemispheres with an imbalance of only 0.4 W m^{-2}, with strong warming contributions evident in the SH subtropics, as also identified as being key in Figs. 2, 3. These experiments therefore show that rapid adjustments are likely an important contributor to the patterns in unmitigated simulations and to injection mass contrasts between GLENS-SAI and ARISE-SAI-1.5, as CO_2 levels continue to increase in these simulations. Moreover, the radiation contrasts can be linked to rapid adjusments in clouds, with reductions in cloud amount in the southern hemisphere subtropics being closely tied to associated increases in FSNT. It is also notable that the hemispheric contrasts in the slow responses to warming also contrast significantly between models, with the pattern in CESM1 being hemispherically asymmetric and offsetting rapid adjustments, and the pattern in CESM2

being approximately symmetric (Fig. S4). While regional features are more difficult to interpret in fully coupled simulations due to the presence of coupled internal variability, it is noteworthy that disproportionate FSNT increases in the NH also emerge in the early years of Abrupt4xCO_2 experiments and these are sustained for several decades. Together these findings highlight the need to understand the sensitivity of the climate response directly to CO_2 if uncertainties in the implementation of SAI are to be reduced.

Contrasting warming patterns in the Atlantic Ocean are also suggestive of the involvement of an additional important component of the energy budget, the Atlantic Meridional Overturning Circulation (AMOC), which transports heat northward in the Atlantic and redistributes ocean mass, nutrients, salinity, and energy globally (Zhang et al. 2019). Differences between the response in AMOC in our experiments are explored in Figure 5. Changes in the strength of the leading mode of AMOC (Fig. 5a) contrast considerably across the experiments. In GLENS-SAI, the intensity of AMOC increases and this drives an associated enhanced northward transport of heat into the NATL (Fasullo et al. 2018). The strengthening contrasts however with all other simulations considered here (Fig. 5a) and with unmitigated climate projections generally (Zhang et al. 2019, Xie et al. 2021), where AMOC typically weakens during the 21st century. A similar decrease in intensity is evident between ARISE-SAI-1.5 and the unmitigated CESM1-WACCM5-RCP85 and CESM2-WACCM-SSP585. A key driver of AMOC's leading mode is deep water formation in the NATL and in this region simulation of ocean density and salinity also differ substantially between the various experiments. In GLENS-SAI, the subpolar NATL becomes denser and more saline (Fig 5b, 5c) while the subtropical north Atlantic Ocean becomes less dense. These changes accompany increases in evaporation and a net negative surface freshwater flux, which enhances salinity and density (Fasullo et al. 2018). In ARISE-SAI-1.5 the situation is reversed, with the subpolar NATL becoming substantially less dense and fresher, with associated reductions in evaporation (not shown). In ARISE-SAI-1.5, density reductions are evident in the Atlantic at all latitudes below 200 to 500 m due to warming (not shown) and salinity increases are evident south of 40N, patterns that contrast markedly with GLENS-SAI. Causal connections between salinity, density, and AMOC intensity can be complex however and will be discussed further below.

The sensitivity of AMOC to CO_2 and SAI also exists as a key uncertainty. Diagnosing individual drivers of AMOC in fully coupled simulations is extremely challenging given the diversity of thermal, saline, and dynamical processes that drive its changes (Zhang et al. 2019) and achieving a full understanding of contrasts between GLENS-SAI and ARISE-SAI-1.5 is left for future work. However, various changes are simulated that are consistent with having an influence and these include the modulation of salinity and density in the NATL (Zhang et al. 2022), as in ARISE-SAI-1.5 a widespread freshening and decrease in density are simulated, in contrast to salinity and density increases simulated in GLENS-SAI (Fig. S6). A similar salinity contrast is also simulated in future unmitigated simulations using CESM2-WACCM-SSP585 and CESM1-WACCM5-RCP85, and in the CESM2-LE and CESM1-LE, suggesting that the contrast is intrinsic, at least in part, to CAM5 and CAM6 structural contrasts (Fig. S6). This possibility is supported further by rapid adjustments in precipitation to CO_2, as CESM2 simulates systematically weaker reductions in precipitation in the northern extratropics than does CESM1 (Fig. 6), both over the Atlantic Ocean and over much of northern extratropical land where river discharge influences ocean salinity. While neither model simulates changes in rainfall that on their own would weaken AMOC, the potential for negative surface freshwater contributions to offset the elevated buoyancy driven by warming is suggested to differ considerably. More

precise attribution of AMOC changes and their contrasts between experiments likely requires additional targeted experiments, the results here point to a potentially important role for rapid adjustments in the water cycle.

Lastly, a role for the future climate scenario in influencing the latitudinal distribution of SAI injection mass is suggested by the differences between CESM2-LE and CESM2-RCP85 warming and radiation patterns, given the stronger NH warming and FSNT increases east of important sulfate emissions regions in Asia in simulations using RCP85 (negative differences in Figs. 2e, 3e, S1e, S2e). This hypothesis can be explored by examining changes in atmospheric sulfate burdens (Fig. 7), which differ significantly through the 2030-70 period between the experiments used. As discussed previously, comparison across these experiments is complicated by the differences in the scenarios used in each. However, the fact that differences in the sulfate distributions across experiments are both significant and correspond directly to simulated features in radiation and temperature suggests a role as a mediating effect on SAI experiments. In general, simulations that use RCP85 emissions show stronger reductions in burdens than those that use SSP370 (Fig. 7d, e) or SSP585 (Fig. 7c). Given the strong cooling associated with the burdens via their impact on clouds, these differences consistute an anomalous NH warming contribution in the 21st C for RCP85-based experiments (Fig. 7c-e) that thus require additional NH mitigation (Fig. 7f).

4 Discussion and Conclusions

The analysis of our climate intervention and complementary experiments highlights a fundamental and perhaps underappreciated contributor to uncertainties surrounding SAI, the rapid adjustments of the climate system to CO_2. Such adjustments include both the responses of patterns in cloud fields, which drive radiation contrasts between hemispheres, and precipitation, which can influence upper ocean salinity, density, and associated ocean circulations and energy flows. As shown here, the simulation of rapid adjustments can vary considerably across models and resolving these inter-model discrepancies is thus critical in order to better constrain the design parameters of SAI if implemented in nature. Uncertainties in future scenarios must also be reduced in order to winnow the spread across SAI simulations, and progress along this front has been made in recent years with the identification of biases in prescribed CMIP6 emissions (e.g. Paulot et al. 2018, Wang et al. 2021). Notably however, the climate response uncertainty associated with prescribed sulfate emissions is magnified by the broad range with which aerosol indirect effects on clouds as represented across climate models. The inference from the SAI simulations explored here is that the latitude of SAI injections will depend explicitly on ambient anthropogenic emissions of sulfate aerosols and formulation of an SAI strategy should therefore be accompanied by well-defined industrial emissions targets.

There are also important limits on the results shown here. First, they are based on only two climate models, and in many respects these models share physics that is central to the representation of SAI. A broader consideration of structural model uncertainty is therefore warranted and it is likely that key sources of uncertainty, such as cloud-aerosol interactions, are not well-estimated in contrasts between our experiments. A need therefore exists for a broader multi-model effort to realistically depict SAI and its uncertainties and to coordinate associated model development efforts. Notably a vast majority of climate models currently cannot represent the diversity of associated processes and fields simulated in WACCM. Observational efforts to monitor relevant fields and guide model development activities are also crucial if the inherent

risks and uncertainties of SAI are to be understood, quanitified, and reduced to a point where SCI might become a promising risk-mitigation measure.

Acknowledgments

This material is based upon work supported by the National Center for Atmospheric Research (NCAR), which is a major facility sponsored by the National Science Foundation (NSF) under Cooperative Agreement 1852977 and by SilverLining through its Safe Climate Research Initiative. The CESM project is supported primarily by the NSF. Computing and data storage resources, including the Cheyenne supercomputer (doi:10.5065/D6RX99HX), were provided by the Computational and Information Systems Laboratory (CISL) at NCAR. We thank all the scientists, software engineers, and administrators who contributed to the development of CESM2. JF was also supported by NASA Awards 80NSSC17K0565 and 80NSSC22K0046.

Availability Statement

All GLENS-SAI and CESM1-WACCM5-RCP85 simulations are available to the community via the Earth System Grid (see information at www.cesm.ucar .edu/projects/community-projects/GLENS/). Output from the CESM1-LE, CESM2-LE, CESM2-RCP85, CESM2-WACCM6-SSP585, simulations and ARISE-SAI-1.5 simulations is freely available the NCAR Climate Data Gateway at https://doi.org/10.26024/0cs0-ev98 and https://doi.org/10.5065/9kcn-9y79 respectively. CMIP6 data including CESM2-WACCM6-SSP585, 4xCO2AMIP, and 4xAbruptCO_2 simulations are available online (https://esgf-node.llnl.gov/projects/cmip6/).

Author Contributions

Conceptualization: J. T. Fasullo, J. H. Richter

Data curation: J. T. Fasullo, J. H. Richter

Formal analysis: J. T. Fasullo

Funding acquisition: J. H. Richter

Methodology: J. T. Fasullo, J. H. Richter

References

Abiodun, B. J., Odoulami, R. C., Sawadogo, W., Oloniyo, O. A., Abatan, A. A., New, M., ... & MacMartin, D. G. (2021), Potential impacts of stratospheric aerosol injection on drought risk managements over major river basins in Africa. *Climatic Change*, 169(3), 1-19, https://doi.org/10.1007/s10584-021-03268-w.

Andrews, T., Forster, P. M., & Gregory, J. M. (2009). A surface energy perspective on climate change. Journal of Climate, 22(10), 2557–2570. https://doi.org/10.1175/2008JCLI2759.1

Bala, G., Caldeira, K., & Nemani, R. (2010). Fast versus slow response in climate change: Implications for the global hydrological cycle. Climate Dynamics, 35(2-3), 423–434. https://doi.org/10.1007/s00382-009-0583-y.

Banerjee, A., Butler, A. H., Polvani, L. M., Robock, A., Simpson, I. R., & Sun, L. (2021), Robust winter warming over Eurasia under stratospheric sulfate geoengineering–the role of stratospheric dynamics. *Atmospheric Chemistry and Physics*, *21*(9), 6985-6997, https://doi.org/10.5194/acp-21-6985-2021.

Burgess, M. G., J. Ritchie, J. Shapland & Pielke R. Jr. (2021), IPCC baseline scenarios have over-projected CO2 emissions and economic growth. Env. Res. Lett., 16, 014016, https://doi.org/10.1088/1748-9326/abcdd2.

Chiodo, G., & Polvani, L. M. (2019), The Response of the Ozone Layer to Quadrupled CO 2 Concentrations: Implications for Climate. Journal of climate, 32(22), 7629-7642, https://doi.org/10.1175/JCLI-D-19-0086.1.

417 Da-Allada, C. Y., Baloïtcha, E., Alamou, E. A., Awo, F. M., Bonou, F., Pomalegni, Y., ... &
418 Irvine, P. J. (2020), Changes in west African summer monsoon precipitation under stratospheric
419 aerosol geoengineering. *Earth's Future, 8(7)*, https://doi.org/10.1029/2020EF001595.

420 Danabasoglu, G., Bates, S. C., Briegleb, B. P., Jayne, S. R., Jochum, M., Large, W. G., ... &
421 Yeager, S. G. (2012). The CCSM4 ocean component. Journal of Climate, 25(5), 1361-1389,
422 https://doi.org/10.1175/JCLI-D-11-00091.1.

423 Danabasoglu, G., Lamarque, J. F., Bacmeister, J., Bailey, D. A., DuVivier, A. K., Edwards, J., ...
424 & Strand, W. G. (2020), The community earth system model version 2 (CESM2). *Journal of*
425 *Advances in Modeling Earth Systems*, 12(2), https://doi.org/10.1029/2019MS001916.

426 Deser, C., Phillips, A., Bourdette, V., & Teng, H. (2012), Uncertainty in climate change
427 projections: the role of internal variability. *Climate dynamics*, 38(3), 527-546,
428 https://doi.org/10.1007/s00382-010-0977-x.

429 Eyring, V., Bony, S., Meehl, G. A., Senior, C. A., Stevens, B., Stouffer, R. J., & Taylor, K. E.
430 (2016). Overview of the Coupled Model Intercomparison Project Phase 6 (CMIP6) experimental
431 design and organization. *Geoscientific Model Development, 9(5),* 1937-1958,
432 https://doi.org/10.5194/gmd-9-1937-2016.

433 Fasullo, J. T., Tilmes, S., Richter, J. H., Kravitz, B., MacMartin, D. G., Mills, M. J., & Simpson,
434 I. R. (2018), Persistent polar ocean warming in a strategically geoengineered climate. *Nature*
435 *Geoscience*, 11(12), 910-914.

436 Ferraro, A. J., & Griffiths, H. G. (2016), Quantifying the temperature-independent effect of
437 stratospheric aerosol geoengineering on global-mean precipitation in a multi-model ensemble.
438 *Environmental Research Letters, 11*(3), https://doi.org/10.1088/1748-9326/11/3/034012.

Forster, P. M., Andrews, T., Good, P., Gregory, J. M., Jackson, L. S., & Zelinka, M. (2013), Evaluating adjusted forcing and model spread for historical and future scenarios in the CMIP5 generation of climate models. *Journal of Geophysical Research: Atmospheres, 118(3)*, 1139-1150, https://doi.org/10.1002/jgrd.50174

Franke, H., Niemeier, U., & Visioni, D. (2021), Differences in the quasi-biennial oscillation response to stratospheric aerosol modification depending on injection strategy and species. *Atmospheric Chemistry and Physics, 21(11)*, 8615-8635, https://doi.org/10.5194/acp-21-8615-2021.

Gettelman, A., Mills, M. J., Kinnison, D. E., Garcia, R. R., Smith, A. K., Marsh, D. R., ... & Randel, W. J. (2019). The whole atmosphere community climate model version 6 (WACCM6). *Journal of Geophysical Research: Atmospheres*, *124*(23), 12380-12403, 10.1029/2019JD030943.

Golaz, J.-C., Larson, V. E., & Cotton, W. R. (2002). A PDF-based model for boundary layer clouds. Part I: Method and model description. *Journal of the Atmospheric Sciences*, 59, 3540–3551, https://doi.org/10.1175/1520-0469(2002)059<3540:APBMFB>2.0.CO;2.

Hurrell, J. W., Holland, M. M., Gent, P. R., Ghan, S., Kay, J. E., Kushner, P. J., ... & Marshall, S. (2013), The community earth system model: a framework for collaborative research. *Bulletin of the American Meteorological Society, 94(9)*, 1339-1360, https://doi.org/10.1175/BAMS-D-12-00121.1.

Kawatani, Y., Hamilton, K., & Watanabe, S. (2011). The quasi-biennial oscillation in a double CO 2 climate. *Journal of the Atmospheric Sciences*, *68*(2), 265-283, https://doi.org/10.1175/2010JAS3623.1.

461 Kay, J. E., Deser, C., Phillips, A., Mai, A., Hannay, C., Strand, G., ... & Vertenstein, M. (2015).
462 The Community Earth System Model (CESM) large ensemble project: A community resource
463 for studying climate change in the presence of internal climate variability. *Bulletin of the*
464 *American Meteorological Society*, *96*(8), 1333-1349, https://doi.org/.

465 Jackson, L. C., Biastoch, A., Buckley, M. W., Desbruyères, D. G., Frajka-Williams, E., Moat, B.,
466 & Robson, J. (2022), The evolution of the North Atlantic Meridional Overturning Circulation
467 since 1980. *Nature Reviews Earth & Environment*, 1-14, https://doi.org/10.1038/s43017-022-
468 00263-2.

469 Jones, A., Haywood, J. M., Jones, A. C., Tilmes, S., Kravitz, B., & Robock, A. (2021), North
470 Atlantic Oscillation response in GeoMIP experiments G6solar and G6sulfur: why detailed
471 modelling is needed for understanding regional implications of solar radiation management.
472 *Atmospheric Chemistry and Physics*, 21(2), 1287-1304, https://doi.org/10.5194/acp-21-1287-
473 2021.

474 Kravitz, B., MacMartin, D. G., Visioni, D., Boucher, O., Cole, J. N., Haywood, J., ... & Tilmes,
475 S. (2021), Comparing different generations of idealized solar geoengineering simulations in the
476 Geoengineering Model Intercomparison Project (GeoMIP). *Atmospheric Chemistry and Physics*,
477 21(6), 4231-4247, https://doi.org/10.5194/acp-21-4231-2021.

478 Kravitz, B., & MacMartin, D. G. (2020), Uncertainty and the basis for confidence in solar
479 geoengineering research. *Nature Reviews Earth & Environment*, *1*(1), 64-75, https://doi.org/
480 10.1038/s43017-019-0004-7.

Krishnamohan, K. S., & Bala, G. (2022), Sensitivity of tropical monsoon precipitation to the latitude of stratospheric aerosol injections. *Climate Dynamics, 1-18*, https://doi.org/10.1007/s00382-021-06121-z.

Larson, V. E., (2017). CLUBB-SILHS: A parameterization of subgrid variability in the atmosphere. arXiv:1711.03675v2 [physics.ao-ph].

MacMartin, D. G., Kravitz, B., Tilmes, S., Richter, J. H., Mills, M. J., Lamarque, J. F., ... & Vitt, F. (2017). The climate response to stratospheric aerosol geoengineering can be tailored using multiple injection locations. *Journal of Geophysical Research: Atmospheres*, *122*(23), 12-574, https://doi.org/10.1002/2017JD026868.

MacMartin, D. G., Wang, W., Kravitz, B., Tilmes, S., Richter, J. H., & Mills, M. J. (2019), Timescale for detecting the climate response to stratospheric aerosol geoengineering. Journal of Geophysical Research: Atmospheres, 124, 1233– 1247. https://doi.org/10.1029/2018JD028906.

Maher, N., Milinski, S., & Ludwig, R. (2021). Large ensemble climate model simulations: introduction, overview, and future prospects for utilising multiple types of large ensemble. *Earth System Dynamics*, *12*(2), 401-418, https://doi.org/10.5194/esd-12-401-2021.

Mills, M. J., Richter, J. H., Tilmes, S., Kravitz, B., MacMartin, D. G., Glanville, A. A., Tribbia J. T, Lamarque J-F., Vitt F., Schmidt A., Gettelman A., Hannay C., Bacmeister J. T., and Kinnison, D. E. (2017), Radiative and chemical response to interactive stratospheric sulfate aerosols in fully coupled CESM1(WACCM). *Journal of Geophysical Research: Atmospheres, 122*, 13,061–13,078, https://doi.org/10.1002/2017JD027006.

National Academies of Sciences, Engineering, and Medicine. Reflecting Sunlight: Recommendations for Solar Geoengineering Research and Research Governance. Washington, DC: *The National Academies Press*., https://doi.org/10.17226/25762, 2021.

Park, S., Bretherton, C. S., & Rasch, P. J. (2014), Integrating cloud processes in the Community Atmosphere Model, version 5. *Journal of Climate*, 27(18), 6821-6856, https://doi.org/10.1175/JCLI-D-14-00087.1.

O'Neill, B. C., Tebaldi, C., Van Vuuren, D. P., Eyring, V., Friedlingstein, P., Hurtt, G., Knutti R., Kriegler E., Lamarque J-F., Lowe J., Meehl G. A., Moss R., Riahi K., and Sanderson B. M., (2016) The Scenario Model Intercomparison Project (ScenarioMIP) for CMIP6. *Geoscientific Model Development*, 9(9), 3461–3482, https://doi.org/10.5194/gmd-9-3461-2016.

Park, S., Bretherton, C. S., & Rasch, P. J. (2014). Integrating cloud processes in the Community Atmosphere Model, version 5. *Journal of Climate*, *27*(18), 6821-6856, https://doi.org/10.1175/JCLI-D-14-00087.1.

Paulot, F., Paynter, D., Ginoux, P., Naik, V., & Horowitz, L. W. (2018). Changes in the aerosol direct radiative forcing from 2001 to 2015: observational constraints and regional mechanisms. *Atmospheric Chemistry and Physics, 18(17),* 13265-13281, https://doi.org/10.5194/acp-18-13265-2018.

Pinto, I., Jack, C., Lennard, C., Tilmes, S., & Odoulami, R. C. (2020), Africa's climate response to solar radiation management with stratospheric aerosol. *Geophysical Research Letters*, 47(2), e2019GL086047, https://doi.org/10.1029/2019GL086047.

Richter, J. H., Tilmes, S., Mills, M. J., Tribbia, J., Kravitz, B., MacMartin, D. G., Vitt, F., and Lamarque J-F. (2017), Stratospheric dynamical response and ozone feedbacks in the presence of

SO2 injections. *Journal of Geophysical Research: Atmospheres, 122*, 12,557–12,573, https://doi.org/10.1002/2017JD026912.

Richter, J., D Visioni , D G. MacMartin , D A. Bailey , N. Rosenbloom , W. R. Lee , M. Tye , & Lamarque, J-F (2022), ARISE Assessing Responses and Impacts of Solar climate intervention on the Earth system with stratospheric aerosol injection (ARISE-SAI), *Geoscientific Model Development*., submitted.

Rodgers, K. B., Lee, S. S., Rosenbloom, N., Timmermann, A., Danabasoglu, G., Deser, C., ... & Yeager, S. G. (2021), Ubiquity of human-induced changes in climate variability. *Earth System Dynamics*, *12*(4), 1393-1411, https://doi.org/10.5194/esd-12-1393-2021.

Samset, B. H., Myhre, G., Forster, P. M., Hodnebrog, Ø., Andrews, T., Faluvegi, G., et al. (2016). Fast and slow precipitation responses to individual climate forcers: A PDRMIP multimodel study. Geophysical Research Letters, 43, 2782–2791. https://doi.org/10.1002/2016GL068064.

Simpson, I. R., Tilmes, S., Richter, J. H., Kravitz, B., MacMartin, D. G., Mills, M. J., Fasullo J. T., and Pendergrass A. G. (2019), The regional hydroclimate response to stratospheric sulfate geoengineering and the role of stratospheric heating. *Journal of Geophysical Research: Atmospheres*, 124, 12587– 12616, https://doi.org/10.1029/2019JD031093.

Smith, W., & Wagner, G. (2018), Stratospheric aerosol injection tactics and costs in the first 15 years of deployment. *Environmental Research Letters*, 13(12), 124001, https://doi.org/10.1088/1748-9326/aae98d.

Smith, R., Jones P., Briegleb B., Bryan F., Danabasoglu G., Dennis J., Dukowicz J., Eden C., Fox-Kemper B., Gent P., Hecht M., Jayne S., Jochum M., Large W., Lindsay K., Maltrud M.,

545 Norton N., Peacock S., Vertenstein M., Year S. (2010), The Parallel Ocean Program (POP)
546 reference manual, Ocean component of the Community Climate System Model (CCSM), LANL
547 Technical Report, LAUR-10-01853, 141 pp.

548 Sun, W., Wang, B., Chen, D., Gao, C., Lu, G., & Liu, J. (2020), Global monsoon response to
549 tropical and Arctic stratospheric aerosol injection. *Climate Dynamics, 55(7)*, 2107-2121,
550 https://doi.org/10.1007/s00382-020-05371-7.

551 Tilmes, S., Fasullo, J., Lamarque, J. F., Marsh, D. R., Mills, M., Alterskjær, K., ... & Watanabe,
552 S. (2013). The hydrological impact of geoengineering in the Geoengineering Model
553 Intercomparison Project (GeoMIP). *Journal of Geophysical Research: Atmospheres*, *118*(19),
554 11-036, doi: 10.1002/jgrd.50868.

555 Tilmes, S., Richter, J. H., Kravitz, B., MacMartin, D. G., Mills, M. J., Simpson, I. R., ... &
556 Ghosh, S. (2018), CESM1 (WACCM) stratospheric aerosol geoengineering large ensemble
557 project. *Bulletin of the American Meteorological Society*, 99(11), 2361-2371,
558 https://doi.org/10.1175/BAMS-D-17-0267.1.

559 Tilmes, S., MacMartin, D. G., Lenaerts, J., Van Kampenhout, L., Muntjewerf, L., Xia, L., ... &
560 Robock, A. (2020), Reaching 1.5 and 2.0 C global surface temperature targets using stratospheric
561 aerosol geoengineering. *Earth System Dynamics, 11(3),* 579-601, https://doi.org/10.5194/esd-11-
562 579-2020.

563 Visioni, D., MacMartin, D. G., Kravitz, B., Boucher, O., Jones, A., Lurton, T., ... & Tilmes, S.
564 (2021), Identifying the sources of uncertainty in climate model simulations of solar radiation
565 modification with the G6sulfur and G6solar Geoengineering Model Intercomparison Project

(GeoMIP) simulations. *Atmospheric Chemistry and Physics, 21(13),* 10039-10063, https://doi.org/10.5194/acp-21-10039-2021.

Visioni, D., Bednarz, E. M., Lee, W. R., Kravitz, B., Jones, A., Haywood, J. M., and MacMartin, D. G.: Climate response to off-equatorial stratospheric sulfur injections in three Earth System Models - Part 1: experimental protocols and surface changes, EGUsphere, https://doi.org/10.5194/egusphere-2022-401, 2022.

Wang, Z., Lin, L., Xu, Y., Che, H., Zhang, X., Zhang, H., ... & Xie, B. (2021). Incorrect Asian aerosols affecting the attribution and projection of regional climate change in CMIP6 models. *NPJ Climate and Atmospheric Science*, *4*(1), 1-8, https://doi.org/10.1038/s41612-020-00159-2.

Xie, M., Moore, J. C., Zhao, L., Wolovick, M., & Muri, H. (2021), Impacts of three types of solar geoengineering on the North Atlantic Meridional Overturning Circulation. *Atmospheric Chemistry and Physics Discussions*, 1-28, https://doi.org/10.5194/acp-2021-877.

Xu, Y., Lin, L., Tilmes, S., Dagon, K., Xia, L., Diao, C., ... & Burnell, L. (2020), Climate engineering to mitigate the projected 21st-century terrestrial drying of the Americas: Carbon Capture vs. Sulfur Injection. *Earth System Dynamics*, https://doi.org/10.5194/esd-2020-2.

Zhang, R. R. Sutton, G. Danabasoglu, Y.-O. Kwon, R. Marsh, S. G. Yeager, D. E. Amrhein, C. M. Little, (2019), A review of the role of the Atlantic meridional overturning circulation in Atlantic multidecadal variability and associated climate impacts. *Rev. Geophys.* **57**, 316–375 (2019), https://doi.org/10.1029/2019RG000644.

Zhang, Q., Chang, P., Yeager, S. G., Danabasoglu, G., & Zhang, S. (2022), Role of sea-surface salinity in simulating historical decadal variations of Atlantic meridional overturning circulation

588 in a coupled climate model. *Geophysical Research Letters*, 49, e2021GL096922.
589 https://doi.org/10.1029/2021GL096922.

590 Zhao, M., Cao, L., Bala, G., & Duan, L. (2021), Climate response to latitudinal and altitudinal
591 distribution of stratospheric sulfate aerosols. *Journal of Geophysical Research: Atmospheres,*
592 *126*, e2021JD035379. https://doi. org/10.1029/2021JD035379

593

Table 1. Climate model experiments used in this study and their design characteristics.

Ensemble Name	Lateral Resolution	Vertical Levels	# mem	Time Span	Future Scenario	Notes
CESM1-WACCM5-RCP85	0.9ºx1.25º	70	20 (3*)	2006-2030 (2099)	RCP85	*3 members extend to 2099
GLENS-SAI	0.9ºx1.25º	70	20	2020-2097	RCP85+SAI	
CESM2-WACCM6-SSP585	0.9ºx1.25º	70	5		SSP585	
ARISE-SAI-1.5	0.9ºx1.25º	70	10	2035-2069	SSP245+SAI	
CESM1-LE	0.9ºx1.25º	30	40	1920-2100	RCP85	
CESM2-LE	0.9ºx1.25º	32	50	1850-2100	SSP370	*smoothed biomass emissions
CESM2-RCP85	0.9ºx1.25º	32	10	1920-2100	RCP85	
CESM1-AMIP	0.9ºx1.25º	30	1	1979-2005	N/A	
CESM1-4xCO2AMIP	0.9ºx1.25º	30	1	1979-2005	N/A	
CESM2-AMIP	0.9ºx1.25º	32	1	1979-2014	N/A	
CESM2-4xCO2AMIP	0.9ºx1.25º	32	1	1979-2014	N/A	
CESM2-AMIP+4K	0.9ºx1.25º	32	1	1979-2014	N/A	
CESM1-PI	0.9ºx1.25º	30	1	0-1800	N/A	
CESM2-PI	0.9ºx1.25º	30	1	0-2000	N/A	
CESM1-Abrupt4xCO2	0.9ºx1.25º	32	1	0-150	N/A	
CESM2-Abrupt4xCO2	0.9ºx1.25º	32	1	0-150	N/A	

596

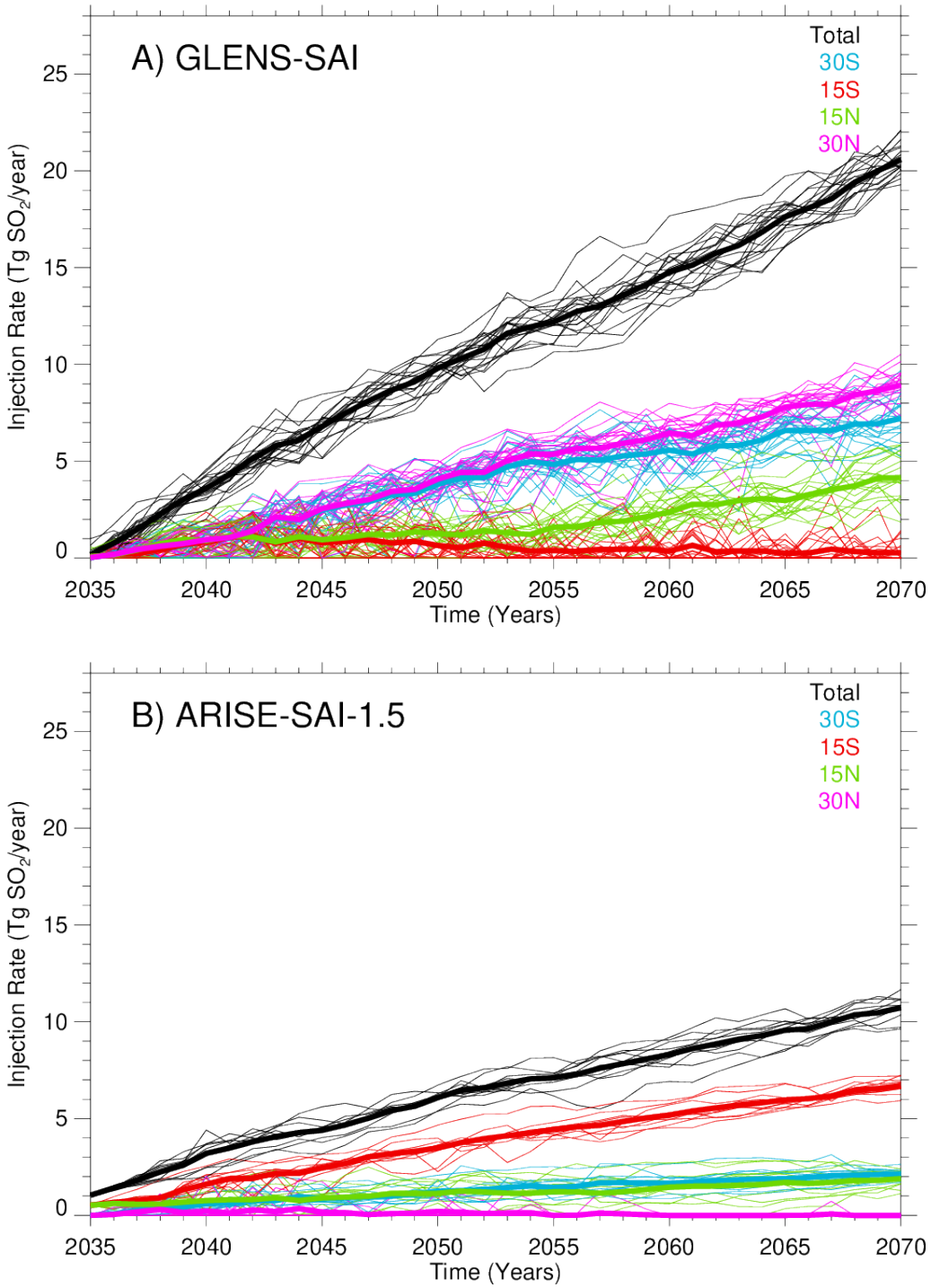

597

598 **Figure 1.** Evolution of yearly sulfur dioxide injections (Tg SO_2 yr^{-1}) over time at the four

599 injection latitudes for (a) GLENS-SAI and (b) ARISE-SAI-1.5 from 2035 to 2070.

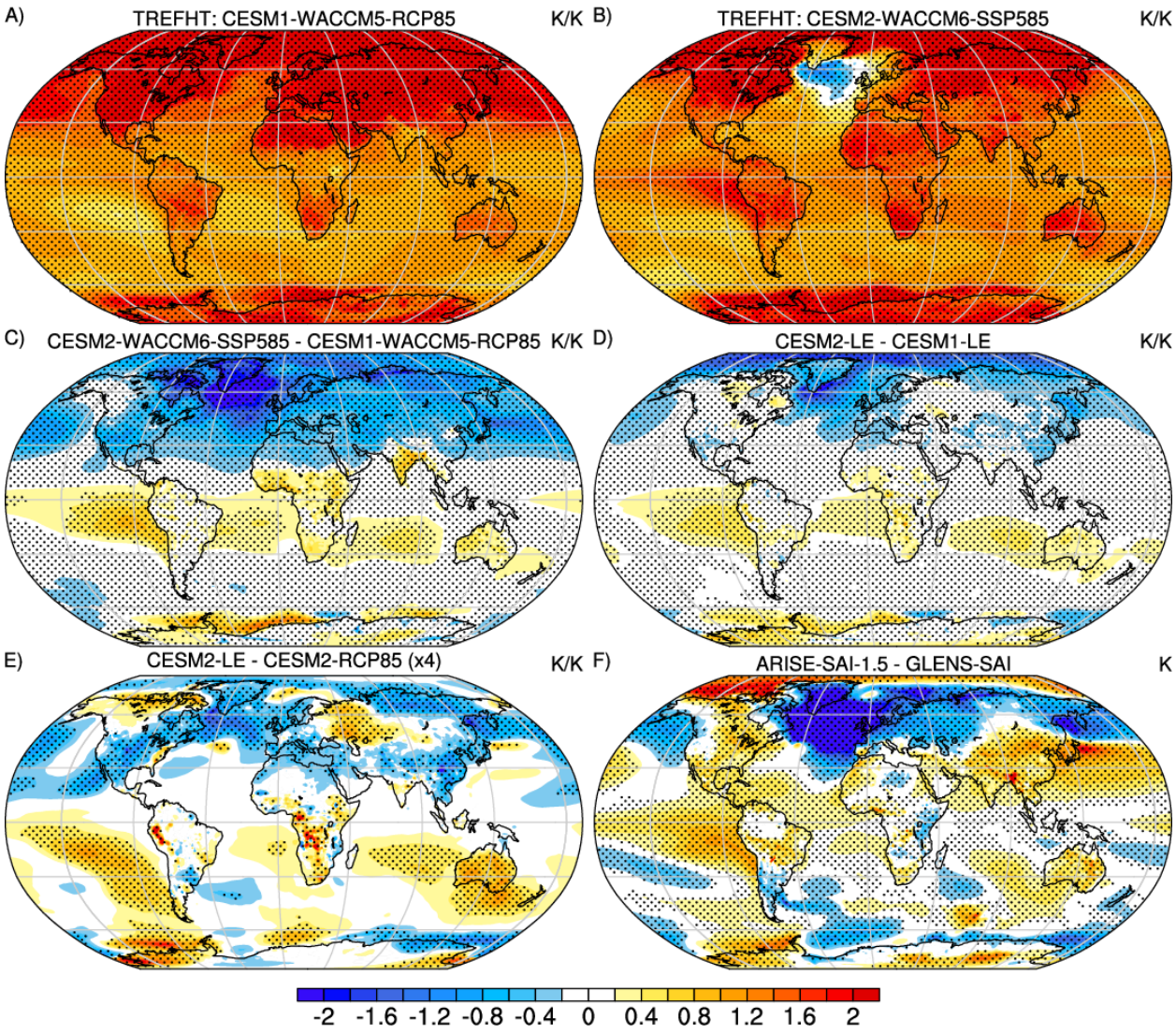

Figure 2. Normalized response in near surface air temperature (TREFHT) estimated from the change between 2020-39 and 2050-69 per degree global warming for unmitigated (a) CESM1-WACCM5-RCP85 and (b) CESM2-WACCM6-SSP585 simulations, and (c) their difference (b-a). Also shown is (d) the analogous difference for the CESM1-LE and CESM2-LE and (e) the CESM2-RCP85 and CESM2-LE (scaled by 4). The difference between the geoengineered climate states in ARISE-SAI-1.5 and GLENS-SAI is shown in (f). Units for all panels are K K^{-1}, except in (f) where units are W m^{-2}, and stippled regions indicate differences that exceed twice the ensemble standard error.

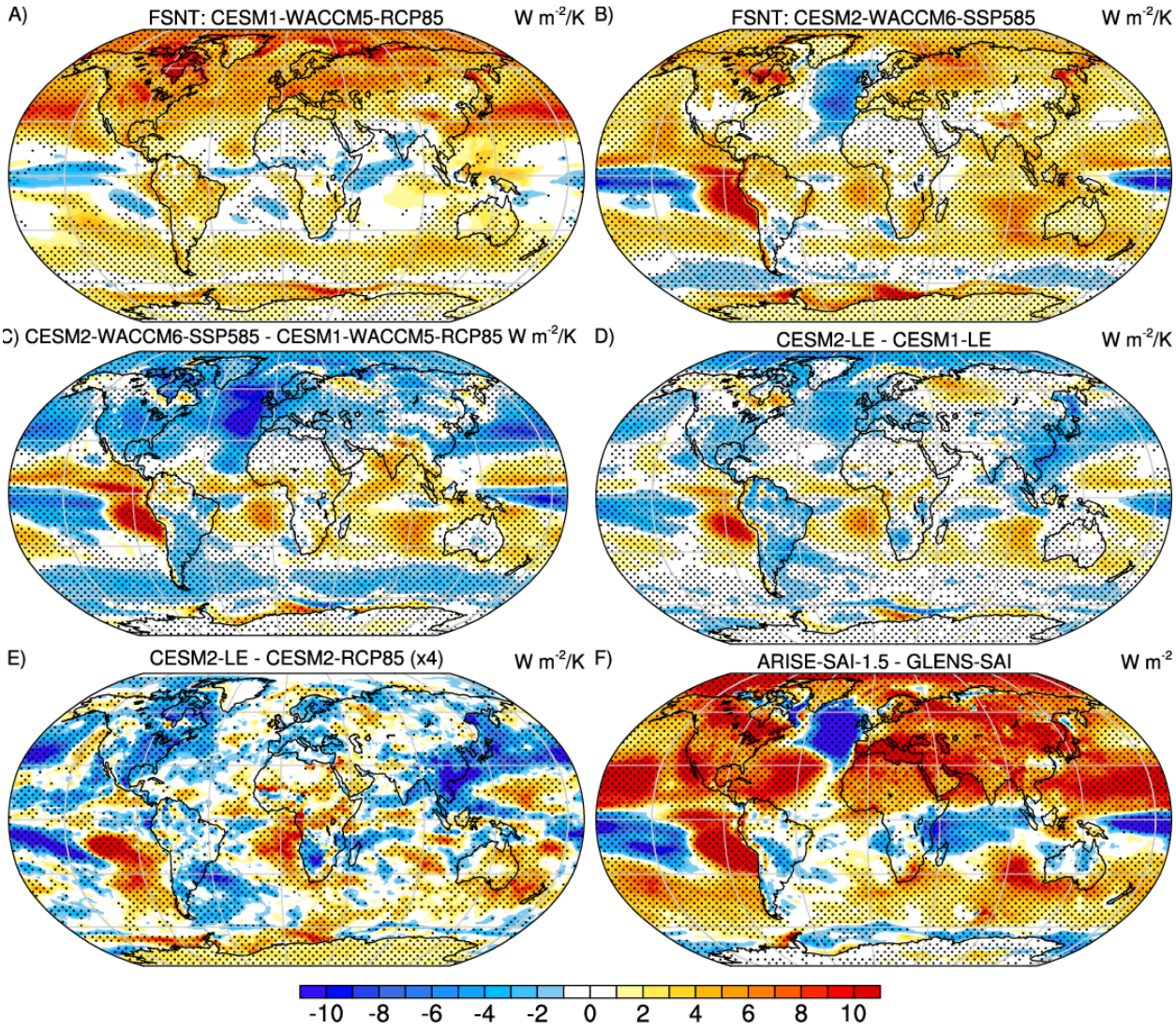

609

610 **Figure 3.** Normalized response in net top-of-atmosphere radiation (FSNT) estimated from the
611 change between 2020-39 and 2050-69 per degree global warming for unmitigated (a) CESM1-
612 WACCM5-RCP85 and (b) CESM2-WACCM6-SSP585 simulations, and (c) their difference (b-
613 a). Also shown is (d) the analogous difference for the CESM1-LE and CESM2-LE and (e) the
614 CESM2-RCP85 and CESM2-LE (scaled by 4). The difference between the geoengineered
615 climate states in ARISE-SAI-1.5 and GLENS-SAI is shown in (f). Units for all panels are W m^{-2}
616 K^{-1}, except in (f) where units are W m^{-2}, and stippled regions indicate differences that exceed
617 twice the ensemble standard error.

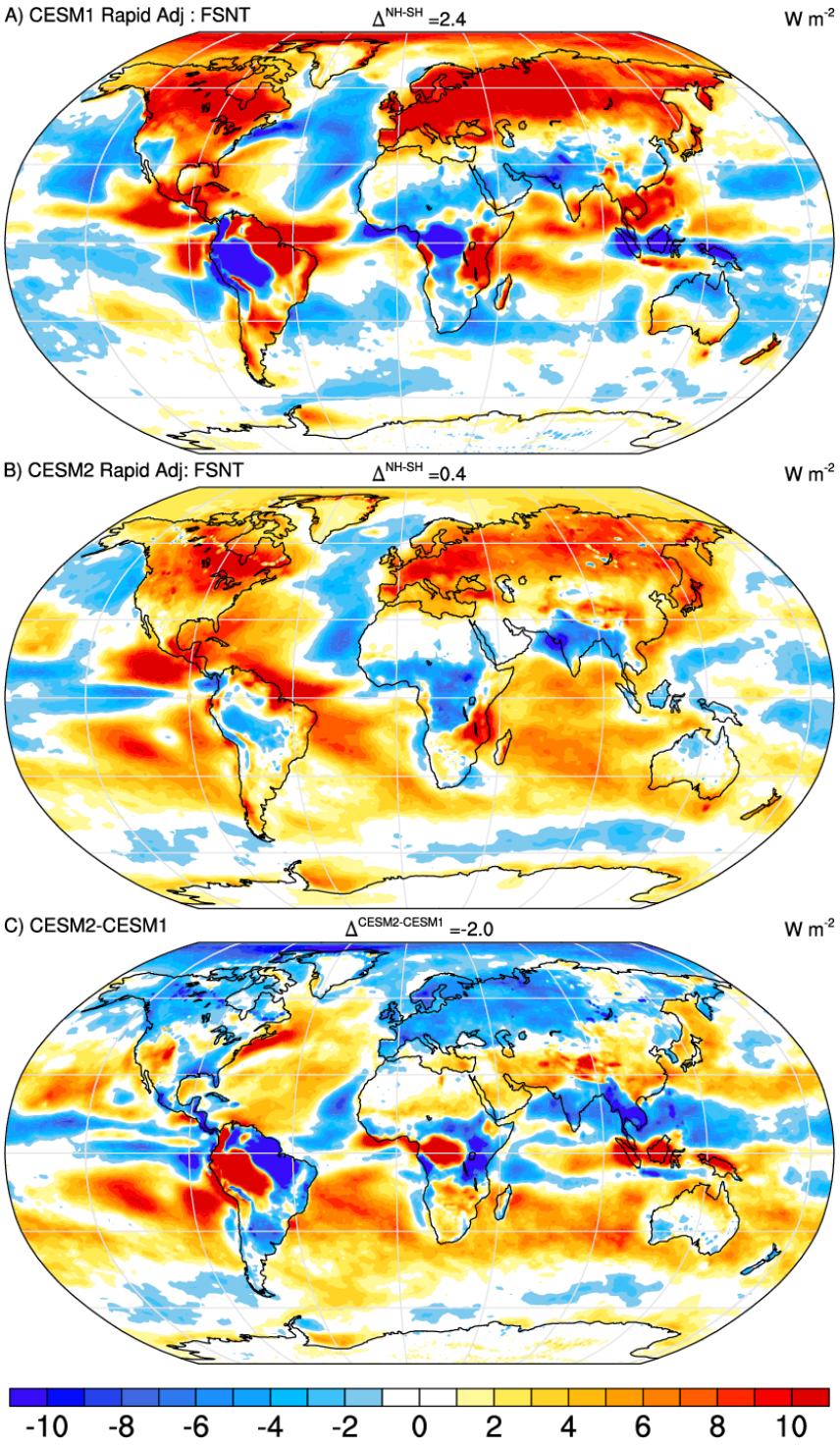

618

619 Figure 4: Estimates of the rapid adjustment of TOA net SW flux to CO_2 for CESM1 (a), CESM2

620 (b), and their difference (c) based on estimates from 4xCO2AMIP and AMIP simulations.

621 Differences in the hemispheric means are shown in panel titles. All units are W m^{-2}.

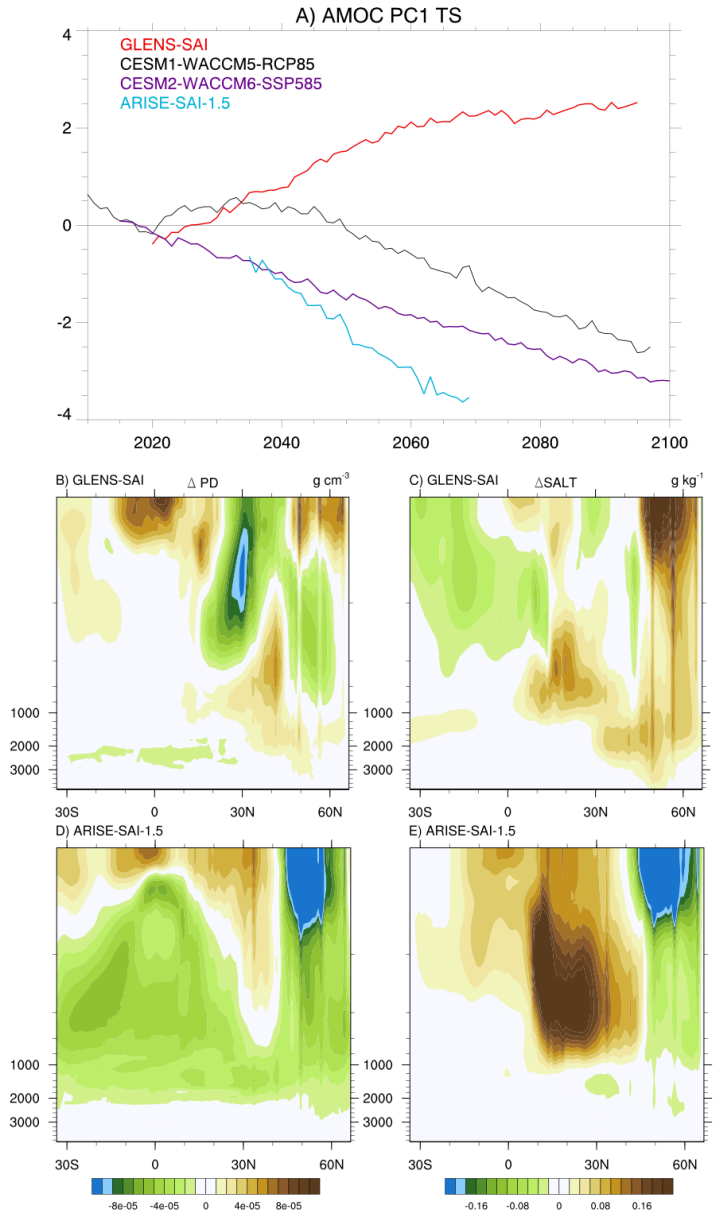

622

623 **Figure 5.** (a) Changes in the leading principal component of the Atlantic Meridional Overturning
624 Circulation in unmitigated (CESM1-WACCM5-RCP85, CESM2-WACCM6-SSP585) and
625 mitigated (GLENS-SAI, ARISE-SAI-1.5) experiments. Also shown are changes in the latitude-
626 depth structure in the Atlantic Ocean of ocean potential density (PD, b, d, units of g cm^{-3}) and
627 salinity (SALT, c, e, units of g kg^{-1}) for GLENS-SAI (b, c) and ARISE-SAI-1.5 (d, e),
628 respectively.

629

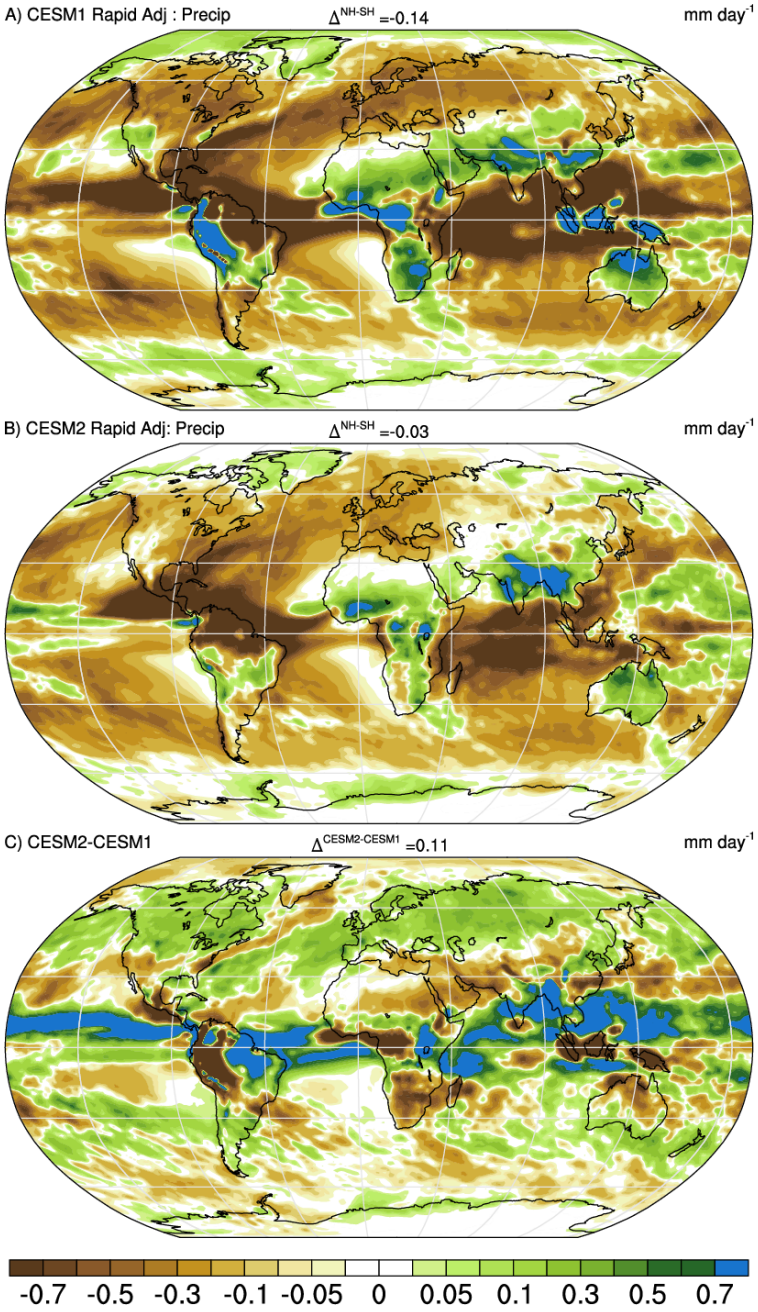

630

631 Figure 6: The rapid adjustment of total precipitation to CO_2 quadrupling for CESM1 (a), CESM2

632 (b), and their difference (c) based on estimates from 4xCO2AMIP and AMIP simulations.

633 Differences in the hemispheric means are shown in panel titles. All units are mm day^{-1}.

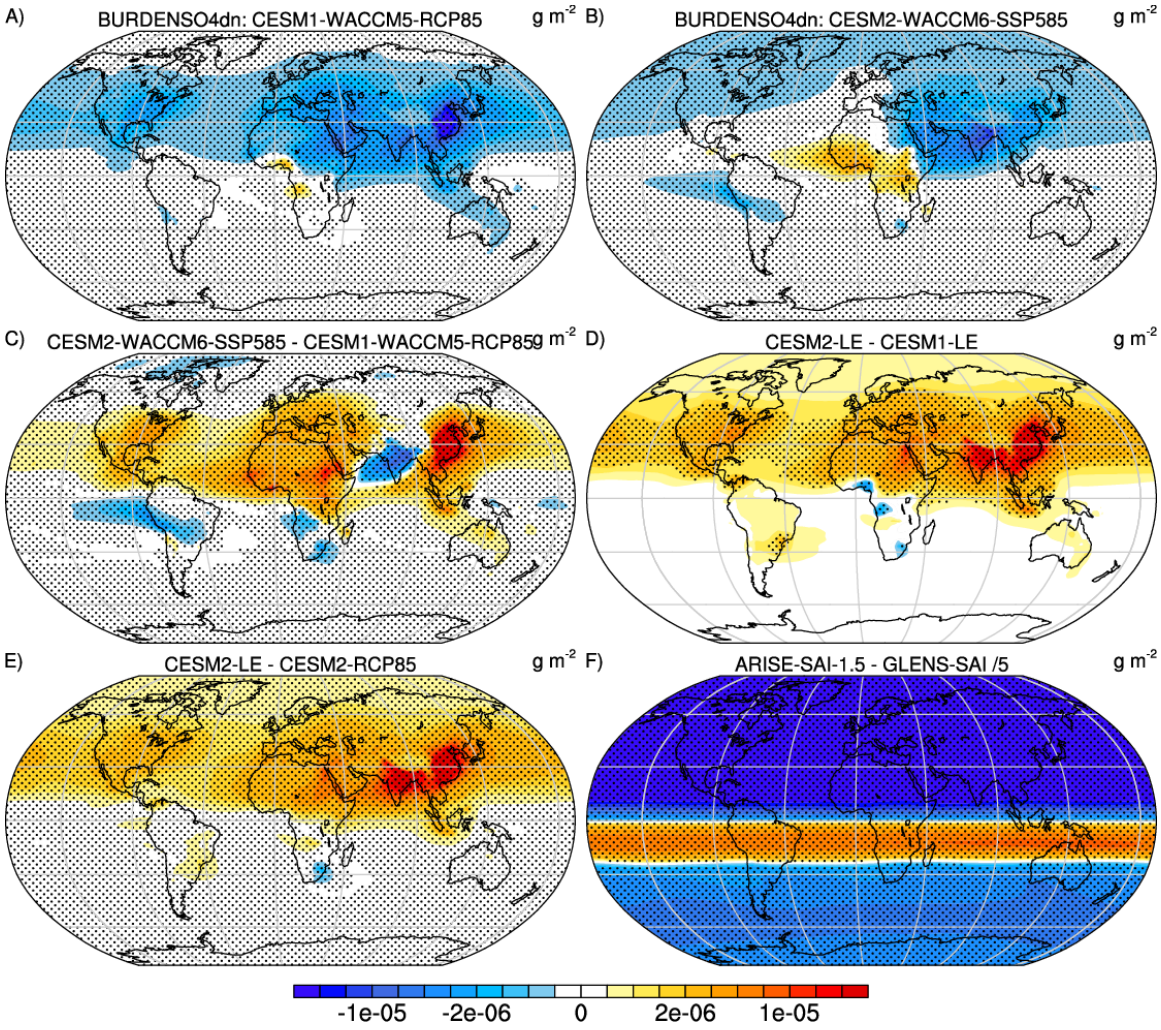

634

635 **Figure 7.** Absolute change in sulfate aerosol burdens (BURDENSO4dn) estimated from the difference
636 between 2020-39 and 2050-69 for unmitigated (a) CESM1-WACCM5-RCP85 and (b) CESM2-
637 WACCM6-SSP585 simulations, and (c) their difference (b-a). Also shown is (d) the analogous difference
638 for the CESM1-LE and CESM2-LE and (e) the CESM2-RCP85 and CESM2-LE. The difference between
639 the geoengineered climate states in ARISE-SAI-1.5 and GLENS-SAI is shown in (f). Units for all panels
640 are g m^{-2} and stippled regions indicate differences that exceed twice the ensemble standard error. The
641 difference field in (f) is scaled by $1/5^{th}$.

642

643

644 **Figure Captions**

645 **Figure 1**. Evolution of yearly injection mass (Tg SO2 yr^{-1}) over time at the four injection
646 latitudes for (a) GLENS-SAI and (b) ARISE-SAI-1.5 from 2035 to 2070.

647 **Figure 2**. Normalized response in near surface air temperature (TREFHT) estimated from the
648 change between 2020-39 and 2050-69 per degree global warming for unmitigated (a) CESM1-
649 WACCM5-RCP85 and (b) CESM2-WACCM6-SSP585 simulations, and (c) their difference (b-
650 a). Also shown is (d) the analogous difference for the CESM1-LE and CESM2-LE and (e) the
651 CESM2-RCP85 and CESM2-LE (scaled by 4). The difference between the geoengineered
652 climate states in ARISE-SAI-1.5 and GLENS-SAI is shown in (f). Units for all panels are K K^{-1},
653 except in (f) where units are W m^{-2}, and stippled regions indicate differences that exceed twice
654 the ensemble standard error.

655 **Figure 3**. Normalized response in net top-of-atmosphere radiation (FSNT) estimated from the
656 change between 2020-39 and 2050-69 per degree global warming for unmitigated (a) CESM1-
657 WACCM5-RCP85 and (b) CESM2-WACCM6-SSP585 simulations, and (c) their difference (b-
658 a). Also shown is (d) the analogous difference for the CESM1-LE and CESM2-LE and (e) the
659 CESM2-RCP85 and CESM2-LE (scaled by 4). The difference between the geoengineered
660 climate states in ARISE-SAI-1.5 and GLENS-SAI is shown in (f). Units for all panels are W m^{-2}
661 K^{-1}, except in (f) where units are W m^{-2}, and stippled regions indicate differences that exceed
662 twice the ensemble standard error.

663 **Figure 4**. Estimates of the rapid adjustment of TOA net SW flux to CO_2 for CESM1 (a), CESM2
664 (b), and their difference (c) based on estimates from 4xCO2AMIP and AMIP simulations.
665 Differences in the hemispheric means are shown in panel titles. All units are W m^{-2}.

666 **Figure 5**. (a) Changes in the leading principal component of the Atlantic Meridional Overturning
667 Circulation in unmitigated (CESM1-WACCM5-RCP85, CESM2-WACCM6-SSP585) and
668 mitigated (GLENS-SAI, ARISE-SAI-1.5) experiments. Also shown are changes in the latitude-
669 depth structure in the Atlantic Ocean of ocean potential density (PD, b, d, units of g cm^{-3}) and
670 salinity (SALT, c, e, units of g kg^{-1}) for GLENS-SAI (b, c) and ARISE-SAI-1.5 (d, e),
671 respectively.

672 **Figure 6**. The rapid adjustment of total precipitation to CO_2 quadrupling for CESM1 (a),
673 CESM2 (b), and their difference (c) based on estimates from 4xCO2AMIP and AMIP
674 simulations. Differences in the hemispheric means are shown in panel titles. All units are mm
675 day^{-1}.

676 **Figure 7**. Absolute **c**hange in sulfate aerosol burdens (BURDENSO4dn) estimated from the difference
677 between 2020-39 and 2050-69 for unmitigated (a) CESM1-WACCM5-RCP85 and (b) CESM2-
678 WACCM6-SSP585 simulations, and (c) their difference (b-a). Also shown is (d) the analogous difference
679 for the CESM1-LE and CESM2-LE and (e) the CESM2-RCP85 and CESM2-LE. The difference between
680 the geoengineered climate states in ARISE-SAI-1.5 and GLENS-SAI is shown in (f). Units for all panels
681 are **g m^{-2}** and stippled regions indicate differences that exceed twice the ensemble standard error. The
682 difference field in (f) is scaled by $1/5^{th}$.

683 **Figure S1**: Normalized response in net top-of-atmosphere radiative flux (RTMT) estimated from the
684 change between 2020-39 and 2050-69 per degree global warming for unmitigated (a) CESM1-

WACCM5-RCP85 and (b) CESM2-WACCM6-SSP585 simulations, and (c) their difference (b-a). Also shown is (d) the analogous difference for the CESM1-LE and CESM2-LE and (e) the CESM2-RCP85 and CESM2-LE (scaled by 4). The difference between the geoengineered climate states in ARISE-SAI-1.5 and GLENS-SAI is shown in (f). Units for all panels are W m^{-2} K^{-1}, except in (f) where units are W m^{-2}, and stippled regions indicate differences that exceed twice the ensemble standard error.

Figure S2: Normalized response in outgoing top-of-atmosphere longwave flux (FLNT) per degree global warming estimated from the change between 2020-39 and 2050-69 for unmitigated (a) CESM1-WACCM5-RCP85 and (b) CESM2-WACCM6-SSP585 simulations, and (c) their difference (b-a). Also shown is (d) the analogous difference for the CESM1-LE and CESM2-LE and (e) the CESM2-RCP85 and CESM2-LE (scaled by 4). The difference between the geoengineered climate states in ARISE-SAI-1.5 and GLENS-SAI is shown in (f). Units for all panels are W m^{-2} K^{-1}, except in (f) where units are W m^{-2}, and stippled regions indicate differences that exceed twice the ensemble standard error.

Figure S3: Rapid adjustments of cloud amount (%) to CO_2 based on 4xCO2AMIP-AMIP simulation differences in (a) CESM1, (b) CESM2, and (c) their difference (b-a).

Figure S4: Slow responses of FSNT (W m^{-2}) to CO_2 estimated from abrupt4xCO2 simulations in CESM1 (a), and computed directly from AMIP+4K-AMIP simulation differences in CESM2 (b). The hemispheric contrasts are large for CESM1 (-2.3 W m^{-2}) and small for CESM2 (0.1 W m^{-2}).

Figure S5: Timeseries of hemispheric mean fluxes (a) and their differences (b) in abrupt4xCO2 simulations.

Figure S6: Response in surface salinity estimated from the change between 2020-39 and 2050-69 for unmitigated (a) CESM1-WACCM5-RCP85 and (b) CESM2-WACCM6-SSP585 simulations, and their difference (c). Also shown is the analogous difference for (d) the CESM1-LE and CESM2-LE (d) and (e) the CESM2-RCP85 and CESM2-LE. The difference between the geoengineered climate states in ARISE-SAI-1.5 and GLENS-SAI is shown in (f).

Figure S7: Rapid adjustments of precipitation (mm day^{-1}) to CO_2 based on 4xCO2AMIP-AMIP simulation differences in (a) CESM1, (b) CESM2, and (c) their difference (b-a).